



Design and optimization of fully differential capacitive MEMS accelerometer based on surface micromachining

Mansour Keshavarzi¹ · Javad Yavand Hasani¹ 

Received: 9 June 2018 / Accepted: 3 October 2018 / Published online: 17 October 2018
© Springer-Verlag GmbH Germany, part of Springer Nature 2018

Abstract

In this paper, design and simulation of a single-axial, capacitive, fully differential MEMS accelerometer based on surface micromachining with two proof masses is presented. So far, most surface micromachined capacitive accelerometers offered, employed differential interface circuits to measure capacitor variations. However, in the presented structure, the possibility of fully differential design is realized by dividing the proof mass to two electrically isolated parts that are located on a silicon nitride layer. By utilizing two proof masses and altering outputs and stimulation voltage, parasitic capacitor is reduced and the sensitivity is increased. Moreover, some sensor capacitors are embedded inside the proof mass, so that sensitivity could be increased in the limited area and electrode length could be reduced. Furthermore, analytic equations are derived to calculate the sensitivity, as well to optimize the sensor structure. The designed sensor has been simulated and optimized using COMSOL Multiphysics, where the simulation results show the mechanical and capacitive sensitivity of 29.8 nm/g and 15.8 fF/g, respectively. The sensor size is 1 mm × 1 mm that leads to excellent performance, regarding to the defined figure of merit.

1 Introduction

Microelectromechanical systems (MEMS) are combining electrical and mechanical components in micro scales. MEMS is a technology with high reliability and performance to manufacturing of sensors. MEMS accelerometer is one of the most efficient sensors in the market. Accelerometers can measure inertial force or mechanical stimulation accelerations. Accelerometers are capable of measuring acceleration, tilt, shock, and vibration in many equipment, and can sense acceleration across one, two, or three axes.

Based on method of acceleration sensing, accelerometers are divided into various categories, including capacitive, piezoelectric, piezoresistive, thermal, and tunneling accelerometers. However, none of these accelerometers alone can meet all market needs. Nevertheless, due to the simple structure, high precision, low thermal sensitivity,

static and dynamic response, and low power consumption, the capacitive accelerometers have a relative advantage in comparison with other accelerometers (Mohammed et al. 2017; Yazdi et al. 1998). MEMS capacitive accelerometers have many applications, including in automobiles, consumer electronics, gaming, guidance systems and navigation (Zhou et al. 2012; Xiao et al. 2017).

Conventional accelerometers fabricated by surface micromachining include a proof mass, where acceleration is measured through proof mass motion and variations of the variable capacitor (Mohammed et al. 2017; Kavitha et al. 2016; Szermer et al. 2017). In these cases, differential interface circuits are employed, while achieving fully differential interface circuits is difficult (Luo et al. 2002). Fully differential interface circuits possess further advantages over differential ones, including common mode noise reduction and Common Mode Rejection Ratio (CMRR) and Power Supply Rejection Ratio (PSRR) improvement (Benmessaoud and Nasreddine 2013; Hsu et al. 2011). Another disadvantage of surface micromachining compared to bulk micro-machining accelerometers, is large parasitic capacitor. In surface micromachining accelerometers, since the sensor is implemented on the substrate, a large parasitic capacitance is developed between the proof mass and the substrate.

✉ Javad Yavand Hasani
yavand@iust.ac.ir

Mansour Keshavarzi
en.mansoor44@yahoo.com

¹ School of Electrical Engineering, Iran University of Science and Technology (IUST), Tehran, Iran

In this paper, we propose a new sensor structure in which, the proof mass is divided to two electrically isolated parts that are located on a silicon nitride layer. Using two separate masses, fully differential interface circuit is realized. Moreover, by having two proof masses in this structure, we managed to reduce the parasitic capacitance by varying excitation voltage and output. To achieve this, instead of applying to the fixed electrodes, we applied the excitation voltage to the moving electrodes. By doing this, output parasitic capacitance to the substrate can be reduced and increase sensitivity (Luo et al. 2002).

Some modifications to the structure are performed in this sensor to prevent excessive enlargement of the sensor. One modification is the use of nickel in the accelerometer, instead of poly-silicon. Nickel is a metal with higher density compared to poly-silicon. Hence, the mass could be increased, which results in Brownian noise reduction as well (Abdolvand et al. 2007). Another modification in our designed sensor is implementation of some electrodes inside the proof mass. By doing so, the sensor surface is utilized to the possible extent, while the length of the capacitor's electrodes are reduced to lessen the problems with long electrodes. In this accelerometer, considering the shape of the capacitors and fully differential interface circuits, an equation for sensor sensitivity is obtained using mathematical analysis, and it is further employed to perform sensor optimization.

Sensor size is one of the most important features of a sensor. Obviously, the higher the occupied area, the better its performance through increasing the number of capacitors and mass (Xiao et al. 2016). However, increase of the sensor size, although feasible, contradicts MEMS sensors minimization. Thus, some limitations are imposed in our proposed accelerometer length and width. In this accelerometer, occupied area is targeted to be $1\text{ mm} \times 1\text{ mm}$, which, to our knowledge is less than most works carried out thus far. The design objective is then obtaining optimum sensitivity level for this size.

2 Principle of working a capacitive accelerometer

The working Principle of a capacitor accelerometer can be modeled with a proof mass connected to a spring and a damper. The one-degree of freedom model of the mass-spring-damper accelerometer is shown in Fig. 1. Comb capacitive accelerometer consists of several capacitors with one fixed electrode and one movable electrode. The movable electrode is connected to the proof mass and moves with its motion. When the sensor is exposed to an acceleration, a force equal to the mass multiplied by the acceleration is applied to the proof mass and causes it to be

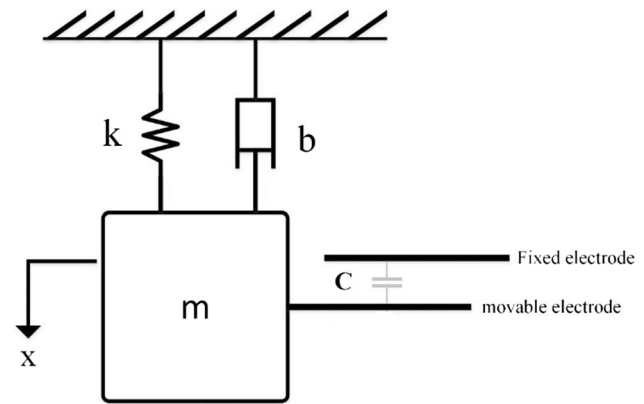


Fig. 1 Mass spring damper model of accelerometer

displaced. This displacement changes the capacitor's gap size, leading to a variations in capacitance. This variations in capacitance can be attributed to the applied acceleration.

This system and the force applied is as a second-order system. By applying the acceleration to the proof mass and according to the second law of motion, the differential equation governing the motion of the device is as follows (Soumendu et al. 2014):

$$m \frac{d^2x}{dt^2} + b \frac{dx}{dt} + kx = ma \quad (1)$$

where x is the proof mass displacement, m is the mass, b is the damping coefficient and k is the spring constant. The resonance frequency of the system is given by (Shahbaz et al. 2017):

$$\omega_f = \frac{k}{m} \quad (2)$$

The MEMS accelerometer works bellow the resonance frequency. In quasi-static state, the proof mass follows acceleration without delays and phase lags. In these conditions, at frequencies much lower than the resonant frequency, the mechanical sensitivity of the sensor is calculated as follows:

$$S_m = \frac{x}{a_{in}} = \frac{m}{k} = \frac{1}{\omega_n^2} \quad (3)$$

According to the above equation, mechanical sensitivity is proportional to the inverse of the resonance frequency square. To increase the mechanical sensitivity of the accelerometer, the resonance frequency of the system should be reduced, which requires an increase in mass and a reduction in spring constant. However, these parameters are limited by the sensor dimensions, since small spring constants reduce mechanical impact resistance, while increasing the mass enlarges the sensor. In addition, reducing the natural frequency reduces the sensor bandwidth. The capacitance accelerometer bandwidth is limited

to several hundred hertz, due to geometrical physics and the air damping around the accelerometer. There is a trade-off between the bandwidth and the accelerometer sensitivity. Applying feedback overcomes this trade-off to some extent.

3 Sensor design

3.1 Proposed sensor structure

In Fig. 2, the overall structure of proposed accelerometer is demonstrated. This accelerometer possess two separated proof masses. The accelerometer structure is symmetrical. The capacitors are embedded within four inner and four outer batches. Moreover, four springs are placed in sensor corners. The structural layer of the sensor is nickel, placed on an insulating layer. The proof mass is divided into two sectors via an air gap, so that the two masses are electrically isolated.

3.2 Spring and mass analysis

In the design of the accelerator spring, a π -shaped spring is utilized (Fig. 3). This spring has the advantage of simplicity. Also, by controlling the dimensions, the spring could be designed to have low spring constant along the sensitive axis, and higher spring constants across other axes. Moreover, this structure embedded a stopper to prevent damage to the spring at high accelerations. The π -

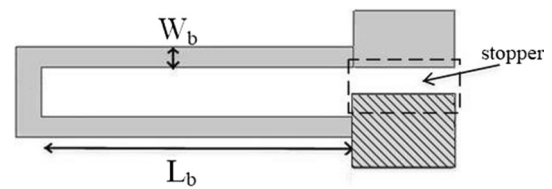


Fig. 3 π -shaped spring structure

shaped spring constant can be obtained from the following formula (Li et al. 2015):

$$k = \frac{1}{2}Et_s \left(\frac{W_b}{L_b}\right)^3 \tag{4}$$

where E is the Young’s modulus for nickel, L_b is the beam length, and W_b is its width. Moreover, t_s is the structural thickness, which is the nickel and the beam layer thickness as well.

As can be seen from Eq. (4), the length and width of the beam have greater impact on the spring constant compared to its thickness. However, increasing the thickness, although increasing the spring constant along the sensitive axis, increases the spring constant across other axes as well, and separates the frequency modes from each other. Equation (4) is given for a spring. According to Fig. 2, four springs are embedded in the structure, so that two springs is connected to each proof mass. The total spring constant for all structure is calculated as the following:

$$k = \frac{1}{2}Et_s \left(\frac{W_b}{L_b}\right)^3 . \tag{5}$$

The accelerometer mass is obtained according to the following equation:

$$m = (\rho_{Ni}t_s + \rho_{ins}t_i)A_p \tag{6}$$

where ρ_{ins} and ρ_{Ni} are ρ_{Ni} nickel and insulating layers density, and A_p is the proof mass area. According to the Eqs. (3), (5), and (6), mechanical sensitivity is calculated as the following.

$$S_m = \frac{x}{a_{in}} = \frac{(\rho_{Ni}t_s + \rho_{ins}t_i)A_p}{4Et_s} \left(\frac{L_b}{W_b}\right)^3 . \tag{7}$$

Mechanical sensitivity indicate proof mass displacement due to acceleration. Therefore, according to Eq. (3), this value can be determined via maximum measurable acceleration and maximum proof mass displacement. Maximum permissible proof mass motion in this accelerometer is considered to be 15% of the capacitive gap, so that the sensor sensitivity stays linear with a good ratio. Moreover, maximum measurable acceleration is taken to be 10 g. In our accelerometer, a number of sensor capacitors are embedded inner the sensor. Although this results in mass reduction, it is compensated by spring constant reduction.

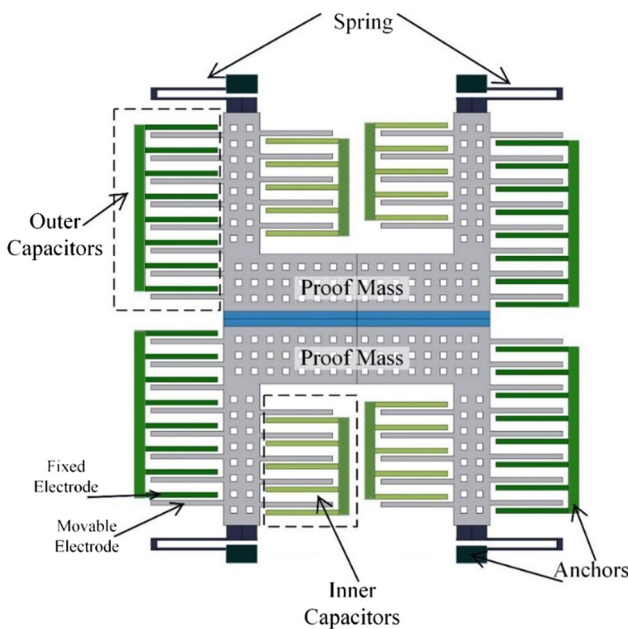


Fig. 2 General structure of the proposed accelerometer

According to Eq. (4), it is possible to decrease the spring constant by increasing the beam length. Now with the gained area, more electrodes can be implemented in the accelerometer to increase sensor sensitivity.

3.3 Interface circuits and sensitivity

There are two methods in order to detect the capacitive variation in MEMS accelerometers (Fig. 4). Most accelerometers fabricated with micromachining technology, employ differential interface circuit (Fig. 4a). In this case, the output detects the capacitor variations. However, fully differential interface circuit possesses advantages over the differential. This is due to two symmetrical outputs, which reduce the common mode noise and offset, improving the power source rejection ratio (PSRR) and the common mode rejection ratio (CMRR). The fully differential mode in the present paper was implemented with two proof masses. In this paper, fully differential mode is implemented via dividing the proof mass into two parts.

Figure 5 demonstrates electrodes structure and capacitors placement. Each set of capacitors consists of two parallel capacitors, one larger than the other. By applying acceleration, the proof mass moves, which results in a change in the main capacitor value C_{1a} . Although the value for secondary capacitor C_{1b} is varied as well, the variation is smaller, given its larger gap relative to the C_{1a} capacitor. If the overlap area of the capacitors is A , and d_1 (gap), and d_2 (anti gap) are the initial capacitance gap for capacitors C_{1a} and C_{1b} , respectively, the capacitance of these two parallel capacitors due to a proof mass displacement with the amount of Δy is as follows:

$$C_1 = C_{1a} + C_{1b} = \frac{\epsilon A}{d_1 \pm \Delta y} + \frac{\epsilon A}{d_2 \mp \Delta y}. \quad (8)$$

Since the dimensions of the capacitors C_2 , C_3 , and C_4 are similar to C_1 , their capacitance is calculated from Eq. (8) as well. Figure 6 depicts the fully differential

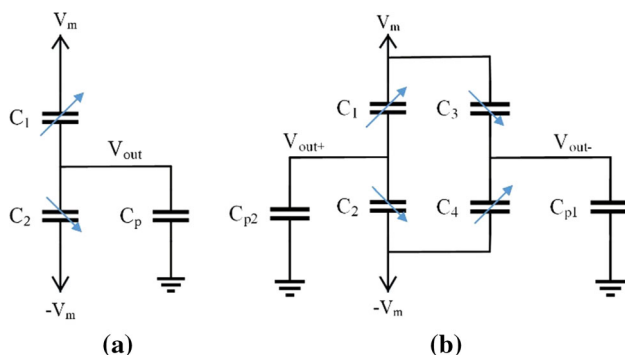


Fig. 4 **a** Differential interface circuit, **b** fully differential interface circuit

interface circuit with all accelerometer capacitors. C_{p1} and C_{p2} are parasitic capacitors.

Fully differential mode capacitance variation for all capacitors is calculated as the following:

$$\Delta C = (N_O + N_i)(C_1 + C_4 - C_2 - C_3) \quad (9)$$

where N_O and N_i are the number of outer and inner capacitors of the sensor, respectively. In the fully differential circuit demonstrated in Fig. 6, assuming $C_1 = C_4$ and $C_2 = C_3$, and by assuming that proof mass displacement relative to the capacitor gap is low, Eq. (9) can be modified as follows:

$$\begin{aligned} \Delta C &= (N_O + N_i) \left[\frac{2\epsilon A \Delta y}{d_1^2 - \Delta y^2} - \frac{2\epsilon A \Delta y}{d_2^2 - \Delta y^2} \right] \\ &\approx 2(N_O + N_i) \epsilon A \Delta y \left(\frac{1}{d_1^2} - \frac{1}{d_2^2} \right). \end{aligned} \quad (10)$$

By taking all capacitors and fully differential circuit into account, capacitive sensitivity of the sensor is obtained as follows:

$$S_C = \frac{\Delta C}{a} = 4(N_O + N_i) \epsilon A S_m \left(\frac{1}{d_1^2} - \frac{1}{d_2^2} \right). \quad (11)$$

The overall sensitivity of the accelerometer is calculated as the following:

$$\begin{aligned} S_t &= \frac{V_{out}}{a} = \frac{V_{out+} - V_{out-}}{a} \\ &\approx \frac{4(N_O + N_i) \epsilon A}{2C_{a0} + 2C_{b0} + C_p} \left(\frac{1}{d_1^2} - \frac{1}{d_2^2} \right) S_m V_m \end{aligned} \quad (12)$$

$$C_{a0} = (N_O + N_i) \frac{\epsilon A}{d_1} \quad (13)$$

$$C_{b0} = (N_O + N_i) \frac{\epsilon A}{d_2} \quad (14)$$

where V_m is the input stimulation voltage. C_{a0} and C_{b0} are the initial capacitors. For sensor's overall sensitivity, number of capacitors, mechanical sensitivity, and stimulation voltage should be increased. However, increasing V_m increases power, which is not a suitable procedure to increase sensitivity. The output voltage could be further enhanced using other circuits.

Parasitic capacitor C_p can result in sensitivity reduction as well. In surface micro-machining accelerometers, since the sensor is implemented on the substrate, a large parasitic capacitance is developed compared to bulk micro-machining accelerometers, which is one of the disadvantages of surface micro-machining. However, in this accelerometer, we were able to reduce this parasitic capacitor. The dominant parasitic capacitor in surface micro-machining is the capacitor between the proof mass and the substrate. As is demonstrated in Fig. 5, it is clear that unlike all surface micro-machining accelerometers, the output is derived

Fig. 5 Placement of sensor capacitors, applied excitation voltage and output voltage

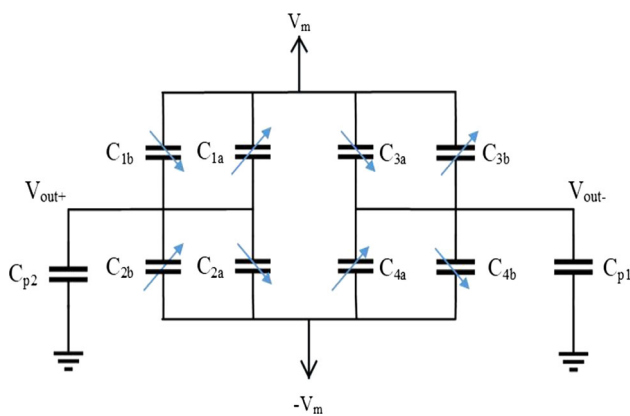
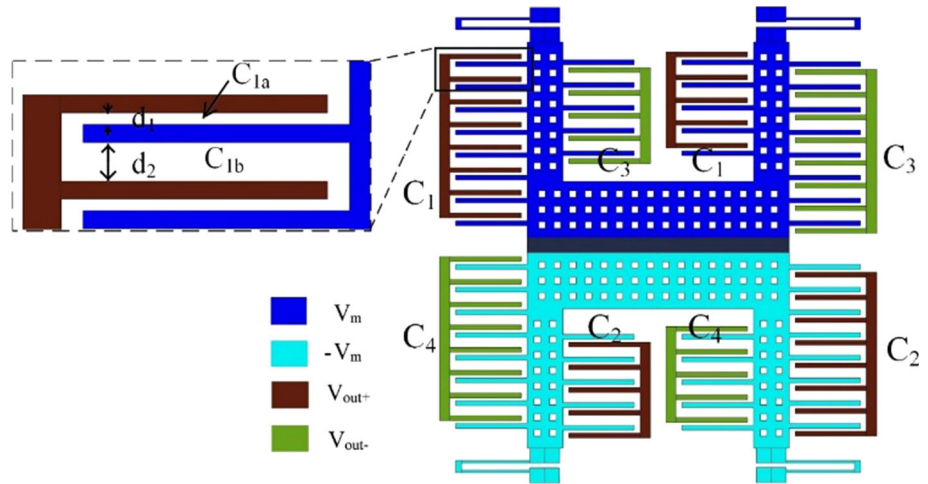


Fig. 6 Fully differential interface circuit of the accelerometer

from the moving electrode, and excitation voltage is applied to the proof mass. This is feasible only by employing two proof masses, which is another advantage of utilizing two proof masses. Under these conditions, parasitic capacitor between proof mass and the substrate could be reduced.

As can be seen in Fig. 5, output voltages V_{out+} and V_{out-} are not obtained from a single side of the sensor. Instead, it is tried to be distributed across all dimensions, to minimize the offset. The same distribution is also applied as far as possible to the capacitors C_1 – C_4 .

It is clear from Eq. (12) that capacitors C_{1b} , C_{2b} , C_{3b} , and C_{4b} decrease the sensitivity. One approach to reduce the effect of these capacitors is increasing the distance d_2 . However, a large increase in d_2 leads to a decrease in the number of capacitors. The curve depicted in Fig. 7 demonstrates the variation in the capacitance versus changes in d_2 . In our proposed accelerometer, the minimum width spacing is considered to be 2 micrometers, and the value of d_1 is also 2 μm . Based on this curve, if the d_2 value is taken about 6 μm , the highest sensitivity level for the sensor is obtained.

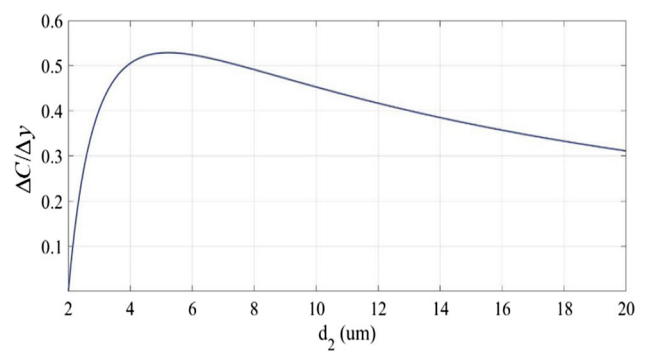


Fig. 7 The effect of d_2 variations on capacitance using Eq. (10)

3.4 Electrodes size

Electrodes size is a crucial parameter in accelerometers determining the capacitance of the capacitors. One fixed electrode of the sensor is demonstrated in In Fig. 8a. The capacitance can be increased via increasing the length (L_e) and thickness (t_e) of the electrode. However, there are limitations to increasing these values. Fixed electrodes move under acceleration as well as movable electrodes. The maximum deflection is for the tip of the electrode as depicted in Fig. 8b. This deflection reduces the sensitivity of the accelerometer, and it should be considered in the

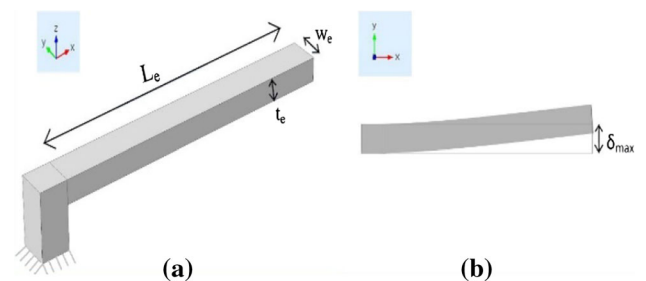


Fig. 8 a The structure of a fixed electrode, **b** fixed electrode deflection due to applying acceleration

design of the electrodes. The maximum deflection is measured using the following equation:

$$\delta_{max} = \frac{12A_{cc}\rho L_e^4}{8EW_e^2} \quad (15)$$

where ρ is density, A_{cc} is the applied acceleration, and W_e is the electrode width. In the above equation, it is clear that the maximum deflection is dependent on the length and width of the electrode, and not on its thickness. In Fig. 9, the maximum deflection of fixed electrode against variations in electrode length for different electrode widths is traced. For the fixed electrodes, maximum deflection must be significantly less than the proof mass displacement. With increasing w_e , although δ_{max} is decreased, but it reduces the number of capacitors installed.

One advantage of installing some of the capacitors inside the accelerometer is to reduce the electrodes lengths. The length of the electrodes can be doubled by reducing the width of the proof mass and installing all capacitors outside it. However, this results in capacitors with long electrodes, and according to Eq. (15), doubling the length of the electrode increases δ_{max} 16 times, which is not desirable for the system. It is also difficult to fabricate long electrodes. In our proposed sensor, by placing part of the sensors inside and halving the length of the electrodes, we have less problems with the length of the electrodes.

3.5 Frequency modes

The shape of the frequency modes can be obtained via sensor modal analysis in COMSOL Multiphysics. One important point in spring design is maintaining spring constant along the sensitive axis less than other axes, so that the first frequency mode could be separated from other modes. Given the simulation results, it is evident that the first and second frequency modes occur across y and z axes, respectively. Hence, frequency mode for z must be higher than y, which is the first mode across the sensitive axis.

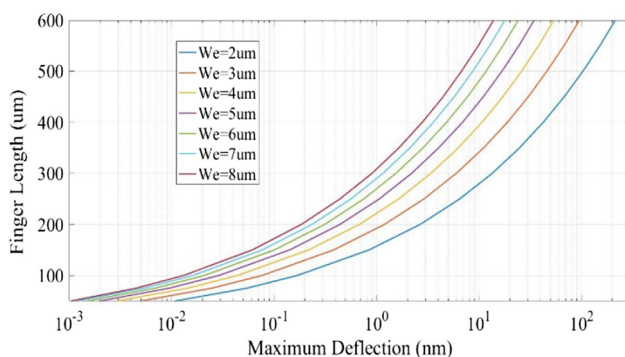


Fig. 9 Maximum deflection curvature (δ_{max}) against variations in electrode length for different electrode widths, derived from Eq. (15)

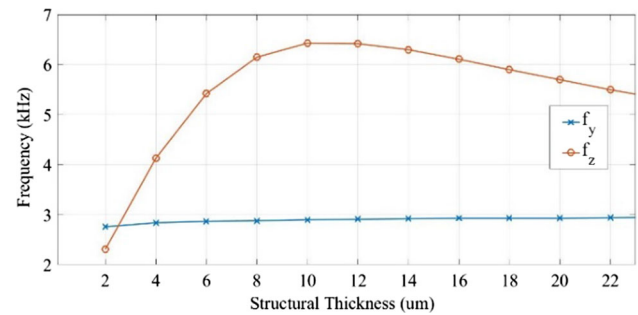


Fig. 10 Frequency modes variation across y and z axes versus structural thickness for spring with $W_b = 2 \mu\text{m}$ and $L_b = 144 \mu\text{m}$, obtained using COMSOL software

To separate these two frequencies, spring dimensions should be modified. The best manner to achieve this is by resizing the sensor's structural thickness. In Fig. 10, the effect of thickness increment on frequency modes of axes y and z is demonstrated. By increasing the structural thickness, although the spring constant is increased across the y axis, the mass is reduced proportionally. Hence, the frequency mode for y is independent of the structural thickness variations. As can be seen, in thicknesses less than $10 \mu\text{m}$, structural thickness increment results in frequency increase across z axis. This is due to the fact that as the structural thickness increases, the spring constant across z axis is incremented as well. However, as the curve confirms, in thicknesses above $10 \mu\text{m}$, f_z declines. This is due to the silicon nitride layer employed to separate the two masses. This layer functions as a spring in high thicknesses, resulting in spring constant and frequency mode reduction across the z axis. Maximum frequency mode separation occurs at thicknesses about $10 \mu\text{m}$.

4 Simulation results

In the following section, simulation results for the designed sensor are presented. COMSOL Multiphysics software is employed to simulate the designed accelerometer. According to simulation results, the obtained mechanical and capacitive sensitivity for the designed sensor are 29.8 nm/g and 15.5 fF/g , respectively. Figure 11 depicts mechanical and capacitive sensitivity curves for the sensor in the 10 g range.

In Fig. 12, the first and second frequency modes for the accelerometer are illustrated. The first accelerometer mode occurs across the y axis, at 2869 Hz . Moreover, the second mode occurs across the z axis at 6412 Hz . In Table 1, geometric parameters and accelerometer characteristics are presented.

In Table 2, a comparison between the performances of designed accelerometers with the performances of other

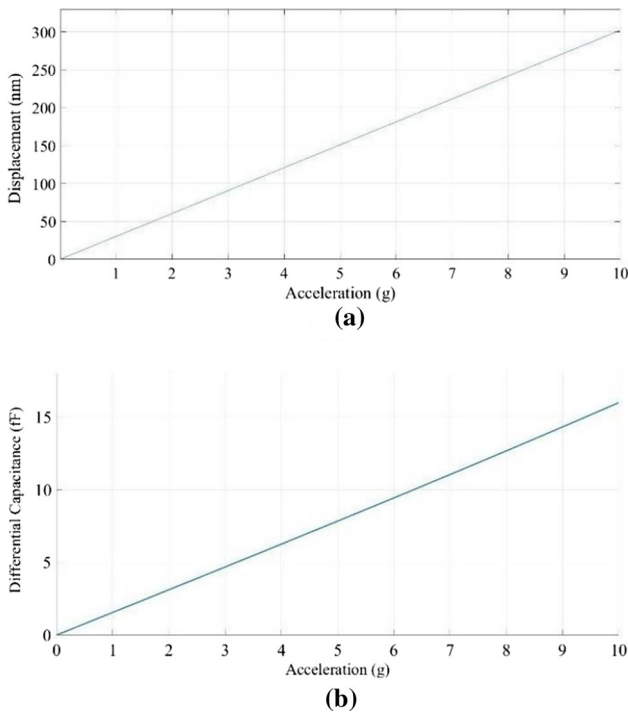


Fig. 11 a Displacement versus acceleration, b differential capacitance versus acceleration

Table 1 Geometric parameters and accelerometer characteristics

Parameter	Symbol	Values
Sensor length and width	$L_s \times W_s$	1 mm×1 mm
Capacitor gap	d_1	2 μm
Capacitor anti gap	d_2	6 μm
Electrodes length and width	$L_e \times W_e$	160 $\mu\text{m} \times 4 \mu\text{m}$
Structural thickness	t_s	10 μm
Spring beam length and width	$L_b \times W_b$	160 $\mu\text{m} \times 2 \mu\text{m}$
Outer number of capacitor	$4 \times N_o$	108
Inner number of capacitor	$4 \times N_i$	68
Mass	m	3.2 μg
Spring constant	k_t	10.72 N/m
Mechanical sensitivity	S_m	29.8 nm/g
Capacitive sensitivity	S_c	15.5 fF/g
1st frequency mode	f_1	2.87 kHz
2nd frequency mode	f_2	6.41 kHz
3rd frequency mode	f_3	13.8 kHz

surface micromachining MEMS accelerometers, is presented. In Table 2 Figure of Merit (FOM) is defined and calculated as the following:

$$FOM = \frac{S_c}{\text{Sensor Area}} \tag{16}$$

The sensor area is the area occupied by the sensor, regardless of packaging and sensor circuits (Fig. 13).

5 Fabrication method and suggestions

In Fig. 14, the proposed method for fabricating a capacitor accelerometer is presented. The proposed fabricating method is entirely based on the conventional methods in MEMS surface micromachining. First, 1 μm oxide is deposited on the substrate to provide isolation between the sensor and the substrate (Fig. 11a). Boron Silicate Glass (BSG) layer is then deposited as the sacrificial layer, and is patterned where anchor is required (Fig. 11b). This layer is removed in the final stage. Following this step, 1 μm silicon nitride, which is the bedding layer for the proof mass, is deposited and patterned (Fig. 11c). Next, a few nanometers thick chromium and gold are deposited using lift-off process to increase adhesion of nickel and the insulating layers (Fig. 11d). Then, the photoresist is deposited and patterned on the surface to fabricate the structural layer. Next, 10 micrometers nickel is electroplated (Fig. 11e, f). Finally, once the photoresist is removed, the sacrificing layer is etched, and the proof mass is released (Fig. 11g, h).

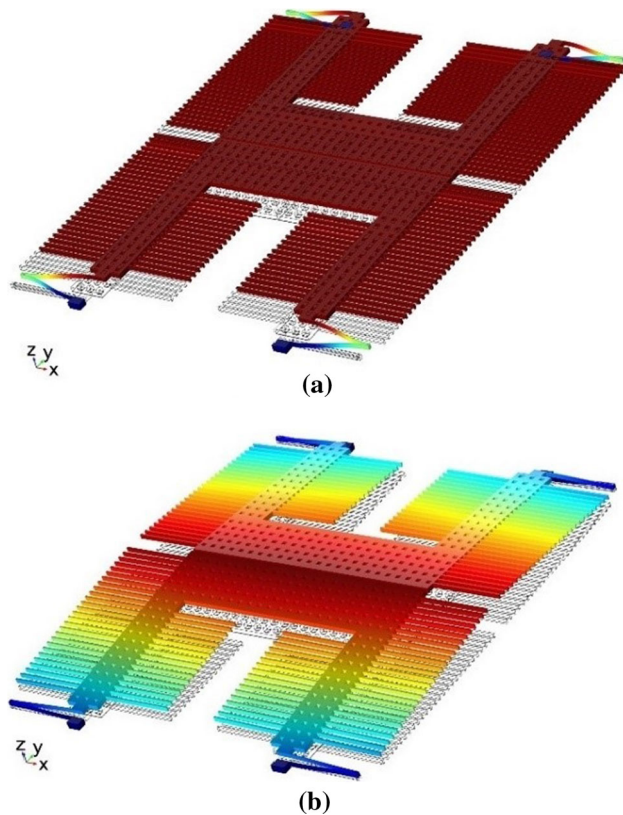
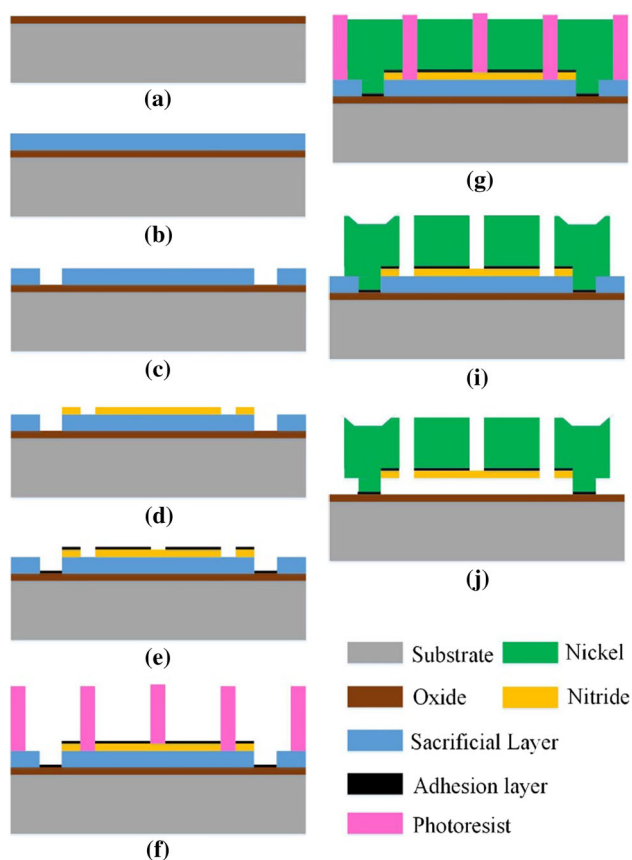


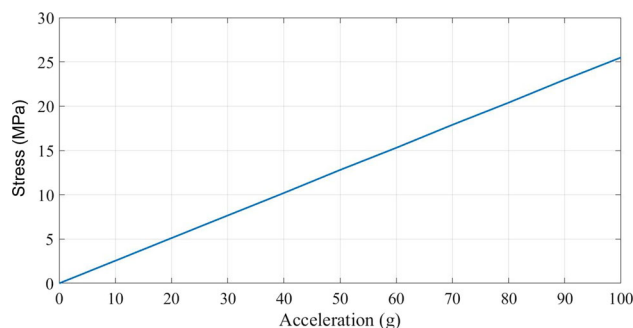
Fig. 12 a First mode frequency, b second mode frequency

Table 2 Comparison of the designed accelerometer with reported surface MEMS accelerometers

References	Resonance frequency (Hz)	Mass (μg)	Mechanical sensitivity (nm/g)	Capacitive sensitivity (fF/g)	Sensor area (mm^2)	Range (g)	FOM
This work	2870	32	29.8	15.51	1	10	20.88
Kavitha et al. (2016) device-A	100	70.5	24	1220	13.4	0.1	91
Kavitha et al. (2016) device-B	500	32.5	1.01	67.5	9.25	2	7.3
Soumendu et al. (2014)	1450	87.4	190	3.83	1.8	10	2.12
Mohammed et al. (2017)	4255	59	13.6	35	4	10	8.75

**Fig. 13** The proposed fabrication method of the accelerometer

The proposed method of fabrication is entirely based on conventional fabricating methods in surface micromachining. These methods include chemical vapor deposition (CVD), electroplating, lift-off and photolithography which is used in the MEMS fabrication. So, there is not any concern about the feasibility of fabrication. However, there is a concern about fracture of thin silicon nitride layer that keeps two parts of the proof mass. Actually, an extreme stress may be applied to this layer under vibration or strong accelerations. To address this concern, we perform a

**Fig. 14** Stress on the silicon nitride versus acceleration in z-axis

simulation and analyze the results. Actually, if acceleration applied in the sensitive axis (y axis), the stress does not affect the silicon nitride layer. For this reason, acceleration in the y axis does not cause any concern about split of two masses. But if a strong acceleration in z-axis applied to the sensor, the related stress is applied to the silicon nitride layer and may cause the split of two proof mass sections. To investigate this case, we performed a new simulation in COMSOL Multiphysics and calculate the stress applied to the silicon nitride layer due to z-axis acceleration. The results are shown in Fig. 14. The results show that under very strong acceleration of 100 g, the applied stress is about 25 MPa. On the other hand, the fracture stress of a 1 μm silicon nitride layer has been measured and reported (Cardinale and Tustison 1992). Based on this report, the fracture stress is at least 390 MPa. Consequently, the maximum worst case stress to the silicon nitride layer in our design is well below the fracture limit.

6 Conclusion

In this paper, a new structure for a capacitive accelerometer based on surface micromachining is presented. In the presented structure, the possibility of fully differential interface is realized by dividing the proof mass into two

mass. Fully differential interface circuits possess further advantages over differential interface circuits, including common mode noise reduction and CMRR and PSRR improvement. By utilizing two proof masses and altering outputs and stimulation voltage, parasitic capacitor is reduced as well. Reducing parasitic capacitance increase sensitivity. Some sensor capacitors are embedded inside the proof mass, so that electrode length could be reduced. In this accelerometer, sensor size is 1 mm × 1 mm, while mechanical and capacitive sensitivity in this limited area are 30 nm/g and 15.8 fF/g, respectively.

Compliance with ethical standards

Conflict of interest The authors declare that they have no conflict of interest.

References

- Abdolvand R, Amini BV, Ayazi F (2007) Sub-micro-gravity in-plane accelerometers with reduced capacitive gaps and extra seismic mass. *J Microelectromech Syst* 16(5):1036–1043. <https://doi.org/10.1109/JMEMS.2007.900879>
- Benmessaoud M, Nasreddine MM (2013) Optimization of MEMS capacitive accelerometer. *Microsyst Technol* 19(5):713–720. <https://doi.org/10.1007/s00542-013-1741-z>
- Cardinale GF, Tustison RW (1992) Fracture strength and biaxial modulus measurement of plasma silicon nitride films. *J Thin Solid Films* 207:126–130
- Hsu YC, Lin CW, Sun CM, Hsu CP, Lee YT, Tsai MH, Liu YC, Fang W (2011) Implementation of fully-differential capacitance sensing accelerometer using glass proof-mass with SI-VIAS. In: *Proceedings of the IEEE international conference on micro electro mechanical systems (MEMS)*, January. IEEE, New York, pp 589–592. <https://doi.org/10.1109/memsys.2011.5734493>
- Kavitha S, Joseph Daniel R, Sumangala K (2016) Design and analysis of MEMS comb drive capacitive accelerometer for SHM and seismic applications. *J Meas* 93(November):327–339. <https://doi.org/10.1016/j.measurement.2016.07.029>
- Li P, Li X, Li E, Shen Q, Chang H (2015) Design and fabrication of an in-plane SOI MEMS accelerometer with a high yield rate. In: 10th IEEE international conference on nano/micro engineered and molecular systems. IEEE, New York, pp 511–514. <https://doi.org/10.1109/nems.2015.7147480>
- Luo H, Zhang G, Carley LR, Fedder GK (2002) A post-CMOS micromachined lateral accelerometer. *J Microelectromech Syst* 11(3):188–195. <https://doi.org/10.1109/JMEMS.2002.1007397>
- Mohammed Z, Dushaq G, Chatterjee A, Rasras M (2017) An optimization technique for performance improvement of gap-changeable MEMS accelerometers. *Mechatronics*. <https://doi.org/10.1016/j.mechatronics.2017.10.011>
- Shahbaz MA, Warsi ZH, Irshad SM, Irshad ST, Jawed SA (2017) Design and analysis of CMOS MEMS based single proof mass tri-axial capacitive accelerometer with readout integrated circuit. In: 2017 First international conference on latest trends in electrical engineering and computing technologies (INTELLECT). IEEE, New York, pp 1–8. <https://doi.org/10.1109/intellect.2017.8277644>
- Soumendu S, Shakya S, Mukhiya R, Gopal R (2014) Design and simulation of MEMS differential capacitive accelerometer. In: *ISSS international conference on smart materials, structures and systems*. <https://doi.org/10.13140/2.1.1074.8809>
- Szermier M, Nazdrowicz J, Zabierowski W (2017) FEM analysis of a 3D model of a capacitive surface-micromachined accelerometer. In: 2017 14th international conference the experience of designing and application of CAD systems in microelectronics (CADSM). IEEE, New York, pp 432–34. <https://doi.org/10.1109/cadsm.2017.7916168>
- Xiao DB, Li QS, Hou ZQ, Wang XH, Chen ZH, Xia DW, Wu XZ (2016) A novel sandwich differential capacitive accelerometer with symmetrical double-sided serpentine beam-mass structure. *J Micromech Microeng* 26(2):25005. <https://doi.org/10.1088/0960-1317/26/2/025005>
- Xiao D, Li Q, Hou Z, Xia D, Xu X, Wu X (2017) A double differential torsional micro-accelerometer based on V-shape beam. *Sens Actuators A* 258(May):182–192. <https://doi.org/10.1016/j.sna.2017.03.011>
- Yazdi N, Ayazi F, Najafi K (1998) Micromachined inertial sensors. *Proc IEEE*. <https://doi.org/10.1109/5.704269>
- Zhou X, Che L, Wu J, Li X, Wang Y (2012) A novel sandwich capacitive accelerometer with a symmetrical structure fabricated from a D-SOI wafer. *J Micromech Microeng* 22(8):85031. <https://doi.org/10.1088/0960-1317/22/8/085031>

Publisher's Note Springer Nature remains neutral with regard to jurisdictional claims in published maps and institutional affiliations.